Modeling of Morphogenesis of Polyolefin Particles: Catalyst Fragmentation

Zdeněk Grof, Juraj Kosek, and Miloš Marek
Dept. of Chemical Engineering, Prague Institute of Chemical Technology, Prague 6, Czech Republic

Pierre M. Adler
IPGP, 75252 Paris Cedex 05, France

The growth of polyolefin particles in heterogeneous catalyzed polymerization reactors is simulated often by reaction-transport models that introduce certain ad hoc effective spatial scales to the description of particle morphology and transport processes inside the particles. Because predictive capabilities of such models with respect to particle morphogenesis are limited, a multiscale model of a growing particle is developed. Maximum relevant information can be systematically extracted from particle microscopy images using the method of reconstructed porous media. The spatially 3-D replicas of the particle pore space allow to calculate the effective transport and mechanical properties. Two new modeling techniques approximate catalyst particle fragmentation: Delaunay triangulation generalized into a 3-D space with non-Euclidean metrics and disconnection of the skeleton representation of the solid phase. Predictive mesoscopic modeling of particle morphogenesis is also discussed.

Introduction

Heterogeneously catalyzed polymerizations of olefins are important industrial processes. The polymerization typically starts from the supported porous catalysts of Ziegler-Natta, chromium, or metallocene type, which are injected into the process as particles with an approx. dia. of 10–50 μm. The stresses induced by the polymer which progressively fills the catalyst pores cause the fragmentation of the catalyst carrier in the early stages of particle growth. Catalyst fragments remain connected by the polymer phase, and this agglomerate forms a porous polymer particle which grows as polymerization proceeds. A fragmentation process is essential for maintaining the sufficiently fast access of the monomer to active catalyst sites originally located within the pores of the support. Since the final polymer particle with 0.2–3 mm dia. contains only a small fraction of catalyst residues, catalyst separation from the polymer particle is usually not required.

The single polymer particle can be viewed as a microreactor, where heat and mass transport, polymerization reactions and various other processes, such as polymer crystallization and particle morphogenesis, take place. The properties of the final polymer product depend not only on the molecular architecture of the polymer (such as chain length distribution, comonomer content, and so on), but also on the morphology of polymer particles, that is, the size and shape of particles and the intraparticle distribution of pore and polymer phases. These properties are greatly affected by the reactor operating conditions and by the architecture of the original catalyst particle. For example, the behavior of Cr/silica catalysts used for ethylene polymerization is strongly influenced by the porosity of the silica support in ways that are not completely understood (McDaniel, 1985; Furtek, 1987; McDaniel et al., 1998). Thus, polyethylene with a lower molecular weight can be produced on silicas having a larger pore-size (Weckhuysen and Schoonheydt, 1999).

The growth of polyolefin particles in heterogeneous catalyzed polymerization reactors is often simulated by reaction-transport models that introduce certain ad hoc effective spatial scales to describe particle morphology and transport processes. Let us mention at least the polymer flow model (for example, Galvan and Tirrell, 1986), the multigrain model (Floyd et al., 1986; Debling and Ray, 1995), and the dusty fluid model (Kosek et al., 2001a). These models proved to be useful for explanation of the particle overheating phe-

Correspondence concerning this article should be addressed to J. Kosek.

nomenon (Hutchinson and Ray, 1987) and discussion of the possible broadening of the molecular weight distribution caused by the resistance against mass transport (Hoel et al., 1994; McKenna et al., 1997). However, the predictive capabilities of these models with respect to particle morphogenesis are limited, especially with regard to the fragmentation of catalyst carriers and early stages of particle growth, which are often believed to be crucial for the formation of final particle morphology (Muñoz-Escalona et al., 1984; Galli, 1994; Estenoz and Chiovetta, 2001). Moreover, the setting of effective mass and heat transport coefficients (diffusivity, permeability, and heat conductivity) in effective-scale models is somewhat arbitrary because of their loose connection to particle morphology. The simple concept of porosity and tortuosity is often employed and the effective transport properties are considered constant during the growth of a polymer particle. Therefore, the calculation of the effective transport properties from the known mesoscopic structure of evolving pore or general multiphase space is addressed in this article.

We attempt to develop a multiscale model of polyolefin particle capable of better understanding the link between the mesoscopic structure of the catalyst and polymer particle and the practical physico-mechanical properties of the final product. Our approach follows a path different from the standard growing particle models—instead of effective spatial scale averaging, we work directly with mesoscopic porous or multiphase media.

The first part of this article is focused on the systematic extraction of information from particle microscopy images by the method of reconstructed porous (or multiphase) media. The spatially three-dimensional (3-D) replica of particle pore space allow us to calculate effective transport and mechanical properties. In the second part of the article, we introduce two techniques suitable for a computationally feasible estimation of the catalyst particle fragmentation: (a) Delaunay triangulation generalized into a 3-D space with a non-Euclidean metrics, and (b) disconnection of the skeleton representation of the solid phase, where the skeleton is obtained by a conditional thinning procedure.

Finally, the outcomes of this mesoscopic modeling are critically discussed and the consecutive steps in the development of complete predictive models of particle morphogenesis are briefly outlined.

Characterization of the Pore Space of Catalyst and Polymer Particles

Thousands of SEM, TEM (scanning and transmission electron microscopy) or other microscopy images (such as X-ray or atomic force microscopy) of catalyst and polyolefin particles are available in industrial and academic research laboratories (Muñoz-Escalona et al., 1984; Kakugo et al., 1989; Galli and Haylock, 1992; Debling and Ray, 2001; Ferrero et al., 1993; Ruddick and Badyal, 1997; Pater et al., 2001). The extraction of quantitative information from these images and systematic linking of this information to the catalyst particle architecture, reaction conditions, and final particle morphology is an important task. Mesoscopic models of growing particles which are closely comparable to quantitative characteristics of actual particle structures could help us in the detailed and rigorous understanding of morphogenesis processes, in the process improvements, in the design of new catalysts, and in the adjustment of properties of final products (Kosek et al., 2001b).

Both catalyst particles used for the polymerization of olefins and the growing polymer particles are porous. Some silica-based catalysts could be produced in the form of a dry powder, while $MgCl_2$-supported catalysts are usually prepared and employed as slurries. $MgCl_2$-supported catalysts are either ball-milled or precipitated, and they may be represented by a complex agglomerate of small crystallites as contrasted with the branched pore network found in silica-supported catalysts (Ferrero et al., 1992).

Results of traditional investigations of porous structures depend on the experimental method being used, such as BET isotherm measurement and mercury intrusion porosimetry give significantly different estimates of specific surface area and average pore-size of the $MgCl_2$ catalyst, cf. Noristi et al. (1994). Moreover, mercury porosimetry could damage the original porous structure and simple intrusion porosimetry can't provide pore-size distribution for most real samples.

As mentioned above, it is necessary to quantitatively characterize these porous media and to estimate the effective transport properties, that is, diffusivity, permeability, and heat conductivity, in order to model the particle growth on an effective scale. The simple approximation of the effective diffusivity D_i^{eff} of the i-th component used in the effective scale models is

$$D_i^{\text{eff}} = \frac{\epsilon}{\tau} D_i \tag{1}$$

where D_i is the bulk diffusivity, ϵ is the particle porosity, and τ is the particle tortuosity. The estimation of Darcy's permeability of the pore space B_0 is typically based on the geometrical model of the porous structure. For example, the Carman-Kozeny relation derived originally for the aggregated bed of spheres gives (Krishna and Wesselingh, 1997)

$$B_0 = \frac{4\langle r \rangle^2}{180} \frac{\epsilon^2}{(1-\epsilon)^2} \tag{2}$$

where $\langle r \rangle$ is the mean pore radius. As can be seen from Eqs. 1 and 2, a porous medium could be characterized in an elementary way by several parameters (porosity, tortuosity, and mean pore radius), and effective properties can be estimated from correlations based on these parameters. However, the choice of tortuosity and mean pore radius is somewhat arbitrary and cannot comprehend peculiarities of many porous structures.

Let us briefly introduce the method of pore space characterization and reconstruction, which generates 3-D representations of a homogeneous pore space (that is, its statistical characteristics are assumed to be independent of the spatial location) by the analysis of 2-D SEM images of the catalyst or polymer particles. At each spatial location $\boldsymbol{x}$ of the porous sample, we can distinguish between the solid-phase and the pore space; we define the phase function $Z(\boldsymbol{x})$

$$Z(\boldsymbol{x}) = \begin{cases} 1 & \text{if } \boldsymbol{x} \text{ belongs to pore space,} \\ 0 & \text{if } \boldsymbol{x} \text{ is in the solid-phase} \end{cases} \tag{3}$$

Statistical averages such as the porosity ϵ and the two-point correlation function of the pore space $R_Z(u)$ can be calculated from the phase function $Z(\boldsymbol{x})$

$$\epsilon = \overline{Z(\boldsymbol{x})} \tag{4}$$

$$R_Z(u) = \overline{[Z(\boldsymbol{x}) - \epsilon][Z(\boldsymbol{x}+\boldsymbol{u}) - \epsilon]}/(\epsilon - \epsilon^2) \tag{5}$$

where the overbar stands for the arithmetic mean overall $\boldsymbol{x}$ and $u = \|\boldsymbol{u}\|$ is the length of the translation vector $\boldsymbol{u}$. The correlation length

$$L = \int_0^\infty R_Z(u)du \tag{6}$$

can serve as a measure of the mean pore-size.

In the first step of the reconstruction process, we binarize a SEM image of a porous medium (see Figure 1a), that is, each pixel of the image is classified according to its color either as a pore space or as a solid. Once the spatially 2-D phase function $Z_{2D}(\boldsymbol{x})$ obtained, the porosity and the correlation function of the binarized image can be computed (see Figure 1b). The SEM images have to be sufficiently homogeneous for the purpose of the reconstruction, that is, the porosities calculated in different sectors of the image should be approximately equal, as well as the correlation functions $R_{Z,x}(u)$ and $R_{Z,y}(u)$ calculated in the x-th and y-th directions, respectively. Moreover, the correlation functions $R_{Z,x}(u)$ and $R_{Z,y}(u)$ shall vanish for large values of u. The correlation function in the x-th and y-th directions are defined by Eq. 5, where the translation vector $\boldsymbol{u}$ is

$$\boldsymbol{u} = \begin{cases} (u,0) & \text{for } R_{Z,x}(u) \\ (0,u) & \text{for } R_{Z,y}(u) \end{cases} \tag{7}$$

The generation of a random phase function $Z_{3D}(\boldsymbol{x})$ possessing the same statistical characteristics (porosity and correlation function) as the experimental phase function $Z_{2D}(\boldsymbol{x})$ (obtained from SEM images) is the key step in the reconstruction process. A noncorrelated random field is generated first; then, it is correlated and discretized by the successive application of linear and nonlinear filters. A more detailed description of this algorithm can be found in literature (Adler, 1992; Adler and Thovert, 1998). Examples of the reconstructed solid phase of the porous medium and its corresponding pore phase are shown on Figures 1c and 1d.

Other alternative algorithms that could be employed for the reconstruction of porous media are Poissonian generation of polydisperse spheres (Thovert et al., 2001) or the method of simulated annealing with the correlation function(s) serving as target(s) (Hazlett, 1997; Yeong and Torquato, 1998). Periodic boundary conditions are usually employed at the opposite walls of the reconstructed cube. The good agreement between the two-point correlation functions of a reference microscopy image and a reconstructed 3-D system does not ensure that the structures of the two systems match well (Biswal et al., 1999; Arns et al., 2001). Other useful two-point characterizations of porous structure include the chord-length distribution function (and the related lineal-path function) and the pore-size distribution function. Different characteristics, such as Minkowski functionals or probability density of the covering radius (Thovert et al., 2001) could be also employed. A 3-D reconstruction of porous silica particles could be also based on the process of its formation, that is, aggregation of colloidal silica in several steps, cf. Kurumada et al. (1998). The 3-D structure of a porous silica particle was also laboriously reconstructed from serially obtained thin microtome sections (Fink et al., 2001).

Effective macroscopic transport properties of reconstructed media can be determined by solving the local transport and balance equations in the pore space. For example, the diffusivity $\boldsymbol{\sigma}$ and the permeability $\boldsymbol{K}$ geometrical tensors could be calculated from the pore space geometry

$$\bar{\boldsymbol{J}} = -D\boldsymbol{\sigma}\cdot\overline{\nabla c}, \quad \bar{\boldsymbol{v}} = -\left(\frac{1}{\mu}\right)\boldsymbol{K}\cdot\overline{\nabla p}, \tag{8}$$

where $\bar{\boldsymbol{J}}$ and $\bar{\boldsymbol{v}}$ are the average molar flux density and the average velocity, $\overline{\nabla c}$ and $\overline{\nabla p}$ are the concentration and the pressure macroscopic gradients, and D and μ are the bulk diffusivity and the viscosity of the fluid, respectively.

Let us discuss the equations and the corresponding boundary conditions used for the calculation of $\boldsymbol{\sigma}$ and $\boldsymbol{K}$ tensors. In order to obtain $\boldsymbol{\sigma}$, the Laplace equation $\nabla^2 c = 0$ with no-flux boundary condition at the solid surfaces of the pores is solved. The arbitrary nonzero concentration difference is applied between two opposite walls in the x-direction of the porous cube, while periodic boundary conditions are employed on the remaining four walls. The average molar flux density vector $\bar{\boldsymbol{J}}$ is then evaluated from the computed concentration field $c(\boldsymbol{x})$. This allows one to obtain the x-column of the diffusivity geometrical tensor $\boldsymbol{\sigma}$. The y- and z-columns are consecutively calculated in an analogous way.

The calculation of the permeability tensor $\boldsymbol{K}$ requires to iteratively solve Stokes equations

$$\nabla p = \mu\nabla^2\boldsymbol{v}, \quad \nabla\cdot\boldsymbol{v} = 0 \tag{9}$$

with the boundary condition of zero velocity $\boldsymbol{v}$ at the pore surfaces. The algorithm for the evaluation of columns of $\boldsymbol{K}$ is analogous to that of $\boldsymbol{\sigma}$ —the pressure difference is consecutively set between opposite walls in the x-, y- and z-directions and the corresponding average velocity field $\bar{\boldsymbol{v}}$ is computed once the solution of Stokes Eqs. 9 is known. The diffusivity and permeability tensors are symmetrical for isotropic porous medium and the effective diffisivity D^{eff} and permeability B_0 are defined as

$$D^{\text{eff}} = \frac{1}{3}Dtr\boldsymbol{\sigma}, \quad B_0 = \frac{1}{3}tr\boldsymbol{K} \tag{10}$$

Several samples were reconstructed using the SEM photographs taken from Niegisch et al. (1992), Kurumada et al. (1998), McKenna et al. (1999), and dos Santos et al. (2001), and transport properties of these media were calculated. The original SEM image, calculated correlation function, and the reconstructed 3-D porous medium of the sample labeled as "DAV02" is illustrated in Figure 1. Percolation of all reconstructed samples was tested. It is also possible to reconstruct nonpercolating porous media of a low or high porosity.

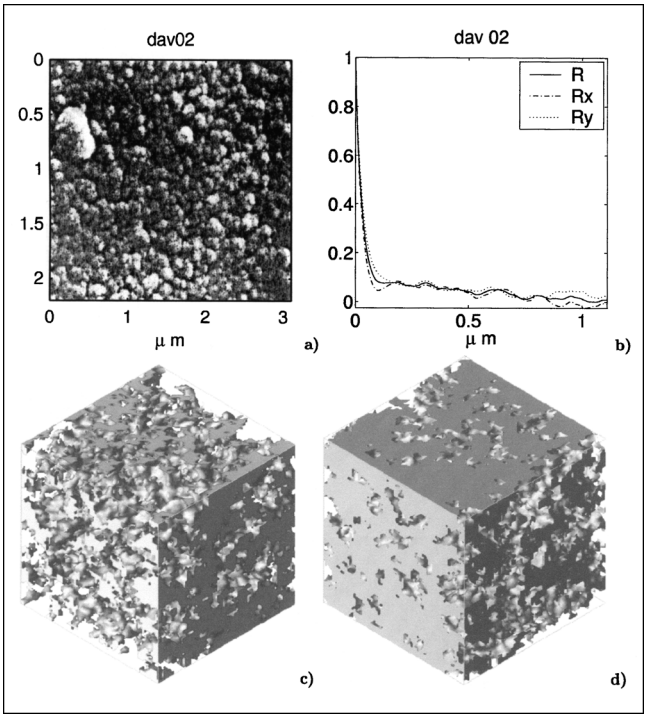

Figure 1. Pore space reconstruction process.

(a) Original SEM image of the catalyst particle "DAV02" from Table 1; (b) correlation function calculated from the SEM image; (c) reconstructed solid phase of the catalyst particle; (d) corresponding reconstructed pore space of the catalyst particle.

Calculated diffusivities and permeabilities of this and other samples are summarized in Table 1. The diffusivity of these samples depends primarily on their open porosity, which is obtained from the total porosity by subtracting the volume of closed cavities formed in the solid phase by the pore space reconstruction algorithm. Both the open porosity and the mean pore diameter (characterized by the correlation length) influence the value of permeability. It should be stressed that effective transport properties presented in this table were calculated with no tunable parameters. If the porous structure is not isotropic, several characteristic sections (SEM images) have to be chosen, their characteristics have to be computed independently and combined in the proper way (Mourzenko et al., 2001).

Table 1. Calculated Transport Properties of Pore Structures Reconstructed from SEM Images*

Sample	ϵ	ϵ_o	σ	B_0/m^2	L/μm
1B1B	0.2495	0.2459	0.0466	9.65×10^{-15}	2.139
1AB	0.2913	0.2884	0.0691	1.68×10^{-14}	2.181
1B1A	0.3329	0.3309	0.0942	2.91×10^{-14}	2.224
DAV01	0.5602	0.5550	0.2834	1.60×10^{-16}	0.045
DAV02	0.6119	0.6111	0.3208	2.89×10^{-16}	0.073
SIL01	0.5108	0.5106	0.2091	1.36×10^{-16}	0.050
SIL03	0.5956	0.5954	0.3098	3.01×10^{-16}	0.052
XER01	0.5892	0.5880	0.2976	5.20×10^{-12}	7.9
XER02	0.6981	0.6976	0.4542	4.87×10^{-12}	4.2

*ϵ is the overall and ϵ_o is open porosity, $\sigma = D^{\mathrm{eff}}/D$ is the ratio of effective and bulk diffusivity, B_0 is the permeability, and L is the correlation length. Smaples 1B1B, 1AB and 1B1A are polymer particles reconstructed from McKenna et al. (1999), DAV01 and DAV02 are silica supports reconstructed from Niegisch et al. (1992), SIL01 and SIL03 are silica supports reconstructed from Kurumada et al. (1998), and XER01 and XER02 are silica supports reconstructed from (dos Santos et al., 2001).

Several studies comparing the calculated transport properties of reconstructed porous media with experimental data were published recently (Bekri et al., 2000) and those comparisons are satisfactory. However, generally, the comparison of measured and calculated transport parameters of porous catalyst particles are still rare. The results of the calculations in Table 1 illustrate some possibilities of a characterization of reconstructed porous media that could be compared with transport properties of experimental samples. Such comparisons are the subject of our future work.

The experimental studies performed by Sliepcevich et al. (2000) in the packed chromatographic column indicate that the characteristic length of diffusion in porous polypropylene particle measured at pressures smaller than in industrial processes is comparable with the particle diameter, that is, it is larger than expected from the framework of the classical multigrain image. However, the result of the pulse solid-gas chromatography might strongly depend upon the elution dynamics and the speed of the response of a detector.

Catalyst Fragmentation

Propylene polymerization on the titanium-compound (Himont) catalyst supported on porous $MgCl_2$ particle under mild polymerization conditions results in the uniform growth of polymer in particle pores and in the homogeneous fragmentation of the catalyst carrier, as it breaks up gradually into smaller and smaller fragments as the polymerization proceeds to yield a multigrain growth (Ferrero et al., 1993; Noristi et al., 1994).

On the other hand, SEM studies of early stages of propylene polymerization on the silica-supported porous catalyst showed the shrinking core model of particle fragmentation (Ferrero and Chiovetta, 1987; Bonini et al., 1995). The polymer starts to grow only in the outer layers of the catalyst particle, clogs the pores, and the fragmentation is relatively slow (Steinmetz et al., 1997; Zechlin et al., 2000). The findings from SEM-images of microtome sections are also supported by kinetic rate profiles of the catalyst, as an induction period corresponding to the particle with polymer-clogged outer layers is observed.

McDaniel (1981) found that the most active Cr/porous-silica catalysts for ethylene polymerization tended to be the most porous and that the fragility of porous supports is essential. He further observed that the fragmentation of the catalyst was complete within the first minute or two of ethylene polymerization. However, Weist et al. (1989) found that the total pore volume alone does not determine the potential performance of a catalyst and is not the only controlling factor in the fracturing process. For example, the 2.3 cm^3/g catalyst support failed to fragment completely, although it has a larger pore volume than the 1.7 cm^3/g catalyst support which fragmented well. Hence, the pore dimensions and the distribution of these within the void network, as well as the rate of polymer formation, controls the fragmentation. The rigid structure of silica supports containing less than 1 cm^3/g pore

volume remains blocked by polymer plugs and the fragmentation does not occur or is very slow (McDaniel et al., 1998). Some experimental studies suggest that the catalyst undergoes continuous fragmentation during the formation of polyethylene with the larger fragments being pushed out toward the surface where the fragmentation continues (Ruddick and Badyal, 1997).

The basic morphological units of polymerization grade silicas such as Davidson 952 appear to be the intermediate, microspheroidal aggregates of 0.05–0.1 μm diameter. The support lattice cracks within the first filling of the pore structure during ethylene polymerization, but the dispersal of the resulting fragments into submicrometer residues is a gradual process which is not yet completed after a five-fold growth of the particle (Niegisch et al., 1992). Conner et al. (1990) employed synchrotron computer microtomography to study ethylene polymerization on silica-supported chromium catalysts and observed that large fragments (>30 μm) are still evident at yields up to 200 g polymer/g catalyst and that polymer particles comprise at least 20–30% voids of dimensions larger than 50 μm.

So far the most detailed phenomenological model of fragmentation during the ethylene polymerization on silica supported chromium catalyst was introduced by Estenoz and Chiovetta (1996). The fragmentation process is modeled as a sequence of discrete steps corresponding to rupture processes in the initial porous carrier. These discrete steps increase the concentration of accessible active catalyst sites.

A rigorous description of the fragmentation process should involve the simulation of pore filling by the polymer, the calculation of the stresses exerted by the polymer on the catalyst support, and the simulation of the formation of fractures in the catalyst support. However, this approach is complex and computationally demanding for realistic samples of catalyst support; for example, the polymer phase is viscoelastic, and the large deformations of the catalyst support and formation of fractures require frequent remeshing. The prediction of the clogging of the pore network by the newly formed polymer in the early stages of the particle growth was discussed by Kosek et al. (2001b).

In this article we approximate the fragmentation process by a geometrical scheme which is computationally more feasible and which approximates the fragmentation. We start from two major assumptions: (i) the fragments are mostly convex objects; and (ii) the surface of the newly formed fractures is minimal. The second assumption neglects the distribution of dislocations in the catalyst carriers since we are trying to locate the bottlenecks of the solid-phase. The algorithm which calculates the location of fractures completely satisfying the two previous criteria will be based on stochastic optimization, and the computational cost of this algorithm is high. Therefore, we propose two simplified algorithms capable of finding only near optimal solutions of the fragmentation problem. The challenging question of the dynamic modeling of the fragmentation process and estimation of its time scale is raised and discussed in the last section.

Two methods of geometrical analysis of fracturing the porous catalyst support were developed: (i) a method based on Delaunay tessellation generalized to 3-D space with non-Euclidean metrics; and (ii) a method disconnecting the "weak" points of the skeleton of the solid-phase obtained by conditional thinning. These algorithms allow us to estimate the number of catalyst fragments, their positions, sizes and catalytic activities, but not the detailed dynamic mechanism of the fragmentation process. The objective of the study is to simply link the structure of porous catalyst support with the final performance characteristics of the catalyst, such as distribution of fragment sizes and their activities.

Fragmentation based on generalized Delaunay tessellation

The starting point is the catalyst support as described by the binary discrete phase function $Z(\boldsymbol{x})$, that is, a binary 3-D matrix. The catalyst carrier consists of the pore space elements and of the solid-phase elements. In the first step, the function $T(\boldsymbol{x})$ specifying the distance of every solid-phase element from the nearest pore element is calculated and this function encodes the bottlenecks of the solid phase structure in a suitable format. Then, in the second step, the propagation of fictious autocatalytic fronts through the solid phase allows us to locate approximate positions of these solid-phase bottlenecks where the fractures are assumed to occur. The purpose of the autocatalytic front is to provide a tool for measurement of distances in complex geometries, cf. Štěpánek et al. (2000).

Two types of non-Euclidean metrics were used for the calculation of distances: (i) "Manhattan" (city block) distance; or (ii) "Chessboard" distance. Let $\boldsymbol{x}_P$ and $\boldsymbol{x}_Q$ be two elements with 3-D coordinates $\boldsymbol{x}_P=(x_P,y_P,z_P)$ and $\boldsymbol{x}_Q=(x_Q,y_Q,z_Q)$. Then, the distance between these two elements $d(\boldsymbol{x}_P,\boldsymbol{x}_Q)$ is defined as

$$d^{MA}(\boldsymbol{x}_P,\boldsymbol{x}_Q)=|x_P-x_Q|+|y_P-y_Q|+|z_P-z_Q| \qquad \text{Manhattan} \quad (11)$$

$$d^{CH}(\boldsymbol{x}_P,\boldsymbol{x}_Q)=\max\left(|x_P-x_Q|,|y_P-y_Q|,|z_P-z_Q|\right) \qquad \text{Chessboard} \quad (12)$$

Let us note that contrary to Euclidean metric these distances are always integer numbers. The function $T(\boldsymbol{x})$ is defined as the distance of $\boldsymbol{x}$ from the nearest pore element

$$T(\boldsymbol{x})=\min_{\boldsymbol{x}_P}\left(d(\boldsymbol{x},\boldsymbol{x}_P)\right)$$

where $\boldsymbol{x}_P$ belongs to pore space

$$Z(\boldsymbol{x}_P)=1 \qquad (13)$$

where the distance $d(\boldsymbol{x},\boldsymbol{x}_P)$ is either the Manhattan or the Chessboard distance given by Eq. 11 or 12, respectively.

The algorithm used for the calculation of the distance transform $T(\boldsymbol{x})$ is simple. The elements of the phase space $Z(\boldsymbol{x})$ are scanned until all distances from the pore space are calculated. In the first step, we assign the value "0" to elements in $T(\boldsymbol{x})$ corresponding to pore space elements in $Z(\boldsymbol{x})$. In the second step we assign distance "1" to elements in $T(\boldsymbol{x})$ corresponding to the solid phase adjacent to the pore element according to $Z(\boldsymbol{x})$. In the third step we assign distance "2" to each still unassigned solid element in $T(\boldsymbol{x})$ which is adjacent to an element already assigned by "1" in $T(\boldsymbol{x})$. In

the subsequent steps we assign positive integers in an analogous way until there are no unassigned elements in $T(\boldsymbol{x})$. Two elements $\boldsymbol{x}_P$ and $\boldsymbol{x}_Q$ are adjacent if their "Manhattan" or "Chessboard" distance $d(\boldsymbol{x}_P,\boldsymbol{x}_Q)$ is equal to 1. Let us illustrate the difference between the "Manhattan" and the "Chessboard" distance transforms $T^{MA}(\boldsymbol{x})$ and $T^{CH}(\boldsymbol{x})$ on an illustrative example considering the 5×5 square where only the single central element is a pore and all other elements represent the solid-phase

$$Z(\boldsymbol{x}) = \begin{bmatrix} 0 & 0 & 0 & 0 & 0 \\ 0 & 0 & 0 & 0 & 0 \\ 0 & 0 & 1 & 0 & 0 \\ 0 & 0 & 0 & 0 & 0 \\ 0 & 0 & 0 & 0 & 0 \end{bmatrix} \tag{14}$$

$$T^{MA}(\boldsymbol{x}) = \begin{bmatrix} 4 & 3 & 2 & 3 & 4 \\ 3 & 2 & 1 & 2 & 3 \\ 2 & 1 & 0 & 1 & 2 \\ 3 & 2 & 1 & 2 & 3 \\ 4 & 3 & 2 & 3 & 4 \end{bmatrix}$$

$$T^{CH}(\boldsymbol{x}) = \begin{bmatrix} 2 & 2 & 2 & 2 & 2 \\ 2 & 1 & 1 & 1 & 2 \\ 2 & 1 & 0 & 1 & 2 \\ 2 & 1 & 1 & 1 & 2 \\ 2 & 2 & 2 & 2 & 2 \end{bmatrix} \tag{15}$$

The next step of the algorithm consists in finding the local maxima in $T(\boldsymbol{x})$. The elements of $Z(\boldsymbol{x})$ with the same distance to the pores (given by $T(\boldsymbol{x})$) forming a connected set can be grouped into clusters. The elements $\boldsymbol{x}_P=(x_P,y_P,z_P)$ and $\boldsymbol{x}_Q=(x_Q,y_Q,z_Q)$ having the same distance to the pores are adjacent if one of the following conditions holds

$$T(\boldsymbol{x}_P)=T(\boldsymbol{x}_Q) \quad \text{and} \quad d^{MA}(\boldsymbol{x}_P,\boldsymbol{x}_Q)=1 \tag{16}$$

$$T(\boldsymbol{x}_P)=T(\boldsymbol{x}_Q) \quad \text{and} \quad d^{MA}(\boldsymbol{x}_P,\boldsymbol{x}_Q)\le 2 \quad \text{and} \quad d^{CH}(\boldsymbol{x}_P,\boldsymbol{x}_Q)=1 \tag{17}$$

$$T(\boldsymbol{x}_P)=T(\boldsymbol{x}_Q) \quad \text{and} \quad d^{MA}(\boldsymbol{x}_P,\boldsymbol{x}_Q)\le 3 \quad \text{and} \quad d^{CH}(\boldsymbol{x}_P,\boldsymbol{x}_Q)=1 \tag{18}$$

where the condition (Eq. 16) requires that two cubic elements $\boldsymbol{x}_P$ and $\boldsymbol{x}_Q$ are the first nearest neighbors (that is, they are wall adjacent), whereas the conditions (Eq. 17) or (Eq. 18) allows the neighboring cubic elements to be second and third nearest neighbors (that is, edge and corner adjacent), respectively. The cluster is then the set of adjacent elements according to one of the above definitions. The local maximum of $T(\boldsymbol{x})$ can be defined as the cluster of a value j with no adjacent cluster with a value greater than j. The condition (Eq. 16) was used for the "Chessboard" while the condition (Eq. 17) was used for the "Manhattan" metrics, respectively.

The basic idea behind the determination of the fracture locations is the simulation of formal (fictitious) autocatalytic reaction-diffusion front spreading out from the local maxima of $T(\boldsymbol{x})$. The location where two fronts encounter is assumed to be the fracture location. The propagation of the front was implemented by considering the diffusion of a pseudo-species A and its reaction inside the solid-phase of the catalyst. Please note that the spreading of autocatalytic front is only hypothetical and is only used for the solid-phase geometry analysis. A similar concept was applied to the analysis of the tortuosity of the pore space by Štěpánek et al. (2000).

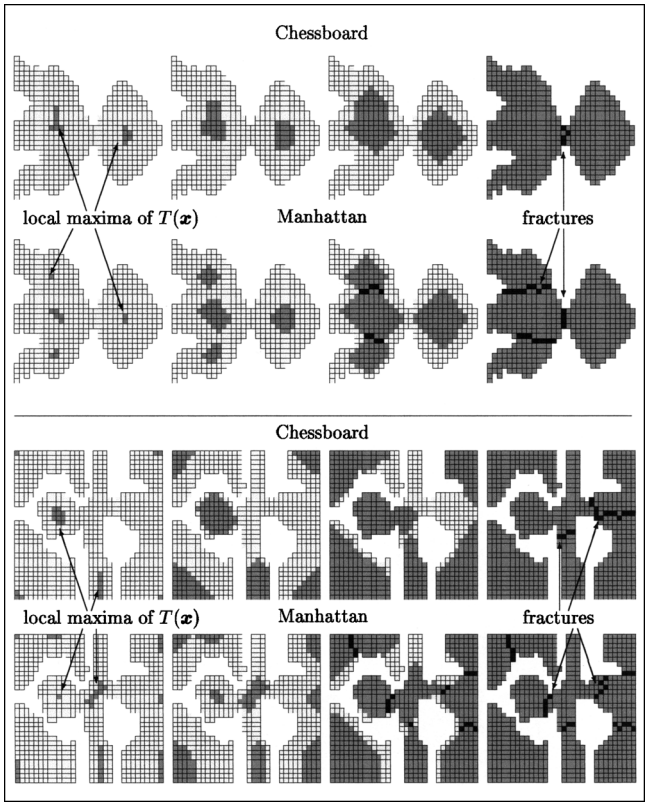

Figure 2. Delaunay tessellation algorithm.

Comparison between the "Manhattan" and the "Chessboard" metrics. The spreading of the reaction-diffusion fronts from local maxima of the distance transform $T(\boldsymbol{x})$ of the original phase function $Z(\boldsymbol{x})$. The solid phase is marked by a light-gray color, the pore space is white, dark-gray color marks the spreading fictious autocatalytic fronts, and black color identifies the fracture locations.

The function of this algorithm is illustrated in Figure 2 on the example of simple 2-D porous structure for both the "Manhattan" and "Chessboard" metrics. The local maxima of the distance transform $T(\boldsymbol{x})$ of the original phase function $Z(\boldsymbol{x})$ are marked by the dark gray color on the left-most pictures in Figure 2. The advance of propagating autocatalytic fronts is shown on consecutive pictures. The fractures, that is, the locations where the distinct fronts meet are marked in a black color on the right-most images in Figure 2.

Let us assume pseudo-species A and B reacting according to the following autocatalytic reaction

$$A + B \rightarrow 2A$$

Let us also assume that these two species are the only species present inside the solid-phase and that they diffuse through the solid-phase, but cannot diffuse into the pore space. The diffusion and consecutive reaction can be described by the

simple partial differential equation

$$\frac{\partial y}{\partial t} = D\nabla^2 y + ky(1-y) \tag{19}$$

where t is the time, y is the mole fraction of species A, D is the local diffusion coefficient, and k is the rate constant. The boundary conditions are defined by the geometry of the solid-phase and by the assumption of no flux through the interface solid–pore phase. The initial conditions are

$$y(t=0) = \begin{cases} 1 & \text{for elements belonging to local maxima of } T(\boldsymbol{x}), \\ 0 & \text{elsewhere in solid and pore phases.} \end{cases} \tag{20}$$

The species A is, thus, present at the start of the simulation only at the local maxima of $T(\boldsymbol{x})$ from which it diffuses to neighboring elements where it reacts. The autocatalytic reaction ensures that the spreading front remains "steep." The propagating front disappears when it reaches the pore space boundary or another propagating front. The propagation of autocatalytic fronts will stop after a certain time as all B is consumed by the reaction.

The diffusion coefficient D in Eq. 19 is a function of the local value of the distance transform $T(\boldsymbol{x})$

$$D(\boldsymbol{x}) = \alpha[T(\boldsymbol{x})]^{\beta} \tag{21}$$

where α and β are tunable parameters. The proper setting of α and β cause the front to advance more quickly in locations which are far from pores than in those near to pores. Since it is advantageous to set the relative high value of β, we used $\beta = 6$ in our simulations. The ratio between α and the rate constant k should keep the spreading front diffusion controlled so the propagating front remains steep.

The parabolic partial differential Eq. 19 was processed by the finite-elements method, where the individual finite elements correspond to elements of the phase function $Z(\boldsymbol{x})$. The record of the actual advance of the propagating fronts during the dynamic simulation is kept in the matrix $R(\boldsymbol{x})$. This matrix helps us to mark the locations where the spreading fronts encounter. In our program code we first assign a distinct positive integer number to every local maximum from $T(\boldsymbol{x})$, store it in $R(\boldsymbol{x})$ and all other elements of $R(\boldsymbol{x})$ are zeroed. Then, we check the value of y in each element during the simulation. When the fraction of species A is close to one (such as, $y > 0.9$) in the element $\boldsymbol{x}_E$, we consider that the autocatalytic front has already passed through it. We also check the values of $R(\boldsymbol{x})$ of all adjacent neighbors of $\boldsymbol{x}_E$ and identify one of the following two cases:

(1) The same positive number g has been assigned to several neighbors of $\boldsymbol{x}_E$ in $R(\boldsymbol{x})$. In this case we assign the value g to $R(\boldsymbol{x}_E)$ and continue in the scanning of propagating fronts or in the integration.

(2) Different positive numbers have been assigned to the neighbors of $\boldsymbol{x}_E$ in $R(\boldsymbol{x})$. This means that two (or more) distinct fronts have met. Hence, we mark the element $R(\boldsymbol{x}_E)$ as the fracture location. Then we continue in the scanning of the remaining elements or in the integration.

When the positive integers are assigned to all elements in $R(\boldsymbol{x})$ corresponding to solid-phase from $Z(\boldsymbol{x})$, the fracture identification process is terminated. Let us note that the number of resulting fragments is the same as the number of local maxima of $T(\boldsymbol{x})$.

Let us note that the "Manhattan" metrics predicts a higher number of catalyst fragments than the "Chessboard" metrics. This difference exists although we implemented condition 16 for the "Chessboard" and condition 17 for the "Manhattan" metric in the search for local maxima of $T(\boldsymbol{x})$. The use of the condition 18, which allows the adjacent cubes to share only one vertex, leads to an even smaller number of fragments [that is, smaller number of local maxima of $T(\boldsymbol{x})$].

Disconnection of the skeleton obtained by conditional thinning

Another method of analysis of the geometry of the porous medium, especially the network connectivity of the pore (or solid) phase, is based on finding the skeleton of the pore (or solid) space. The skeletonization of the porous medium by the homotopic thinning, analysis of its topological characteristics, and determination of connected and percolating components was studied by Thovert et al. (1993).

In a later work, Liang et al. (2000b) extracted the skeleton of pore space using an improved parallel thinning algorithm introduced by Ma and Sonka (1996). Once the skeleton is

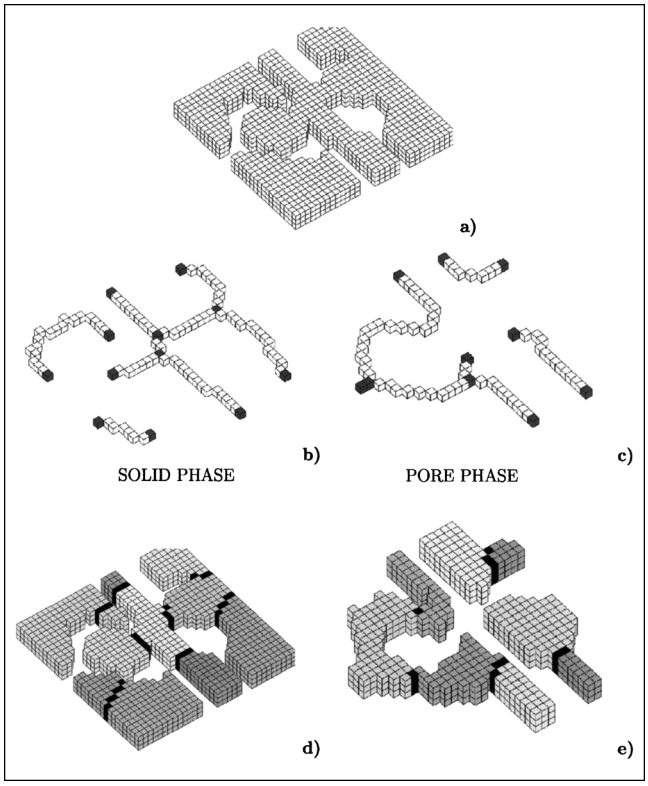

Figure 3. Skeletonization (conditional thinning) and the skeleton disconnection applied to a 2-D porous medium.

(a) Original porous medium, cubes mark the solid phase; (b) skeleton of the solid phase; (c) skeleton of the pores; (d) disconnection of the solid phase at its "weak" points; (e) disconnection of the pore space at its bottlenecks.

Table 2. Geometrically Based Fragmentation Analysis of Porous Samples: Comparison of Different Algorithms*

Sample	Porosity Size of Sample	Method	Number of Fragments	A_P	A_F	A_F/A_P
A	0.37	TH	47	71,050	12,387	0.17
	$64\times64\times64$	MA	325		94,882	1.34
		CH	158		65,856	0.93
D	0.47	TH	104	96,022	14,742	0.15
	$64\times64\times64$	MA	575		92,056	0.96
		CH	326		66,884	0.70
B1	0.20	TH	25	6,652	5,079	0.76
	$64\times64\times8$	MA	36		9,494	1.43
		CH	17		5,798	0.87
C1	0.44	TH	48	9,618	3,178	0.33
	$64\times64\times8$	MA	76		9,126	0.94
		CH	38		4,958	0.52
E2	0.60	TH	35	10,999	1,890	0.17
	$64\times64\times8$	MA	102		6,430	0.58
		CH	59		3,962	0.36
F1	0.32	TH	23	10,888	4,075	0.37
	$64\times64\times8$	MA	118		15,660	1.43
		CH	46		8,724	0.80
F2	0.29	TH	20	8,894	4,343	0.49
	$64\times64\times8$	MA	77		12,232	1.37
		CH	29		5,536	0.62

*A_P is the area of the surface of the original porous sample, A_F is the area of newly formed fractures, TH is the skeletonization based algorithm (conditional thinning); MA is the Delaunay tessellation with the "Manhattan" distance metric; CH is the Delaunay tessellation with the "Chessboard" distance metric.

obtained, its vertices and edges could be identified as well as the minima in the cross-section area of pores along the skeleton branches, which correspond to bottlenecks of the pore space.

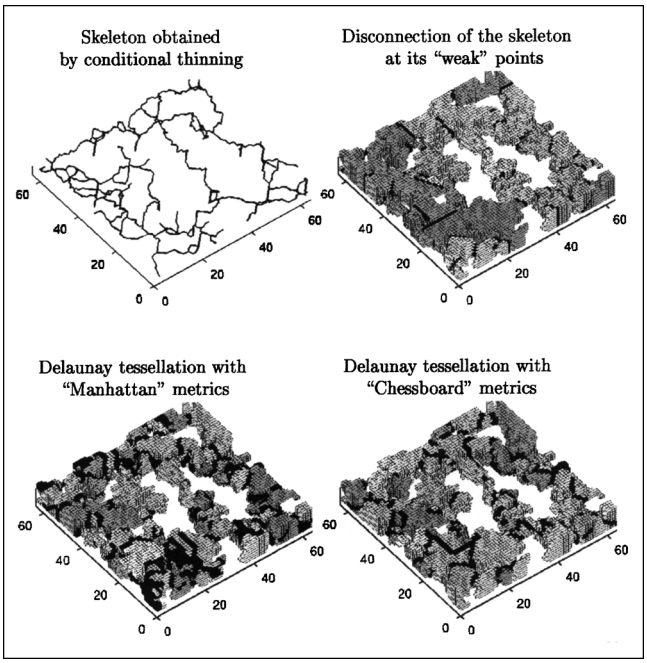

Figure 4. Fragmentation algorithms on the section of the pore space with thickness $64\times64\times8$ (sample "E2" from Table 2).

We applied a similar method not to the pore space, but to the solid phase in order to find the bottlenecks of the skeleton of the solid phase. It is again assumed that the disconnection (fracture) of the solid phase occurs at the "weak" bottleneck points. The skeletonization extracts the information about the topology and the connectivity of the porous object. The elements of the object are removed until only the skeleton remains. This process is called "thinning" in the terminology of mathematical morphology. An illustrative example of the object and its skeleton is shown in Figures 3a and 3b.

We employed the fully parallel 3-D thinning algorithm described by Ma and Sonka (1996) that preserves the original connectivity of the processed phase. During the thinning, an object element is removed if its neighborhood satisfies any of the deleting templates, cf. Ma and Sonka (1996) for details, and thinning ends when no additional object element could be removed. The elements of a resulting skeleton can then be classified as:

(1) *Line-end elements* if they have only one neighboring element;

(2) *Edge elements* if they have two neighboring elements; or

(3) *Vertices elements* if they have three or more neighboring elements.

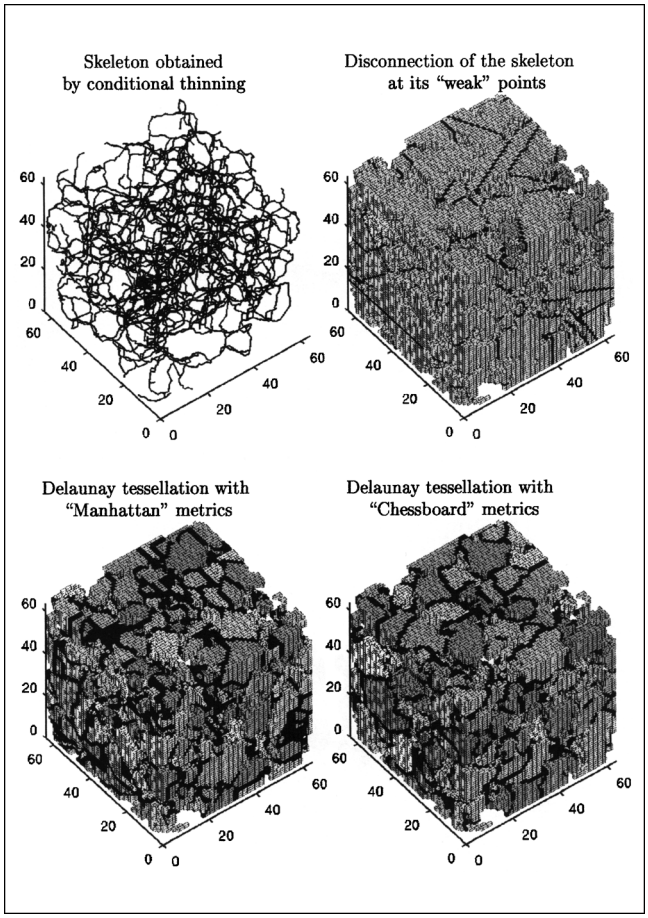

Figure 5. Fragmentation algorithms on the sample of the pore space of the size $64\times64\times64$ (sample "D" from Table 2).

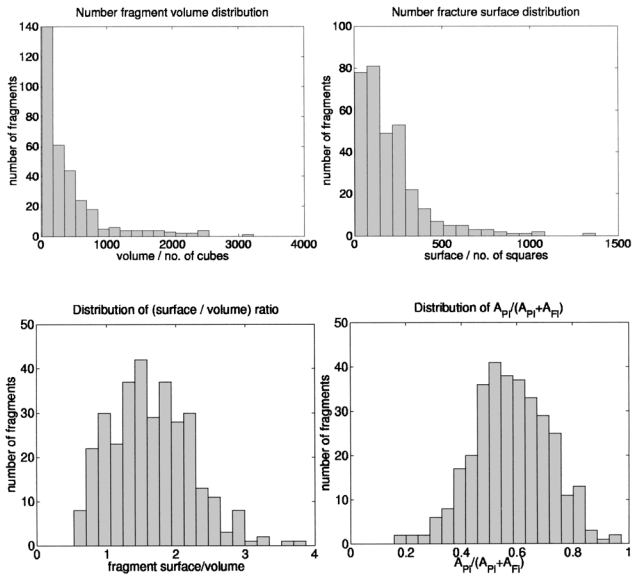

Figure 6. Characteristics of fragments presented as distributions.

Analysis of the sample "D" by Delaunay tessellation with Chessboard metrics. The last histogram shows the average fraction of fragment surface potentially covered by the catalyst, $A_{pi}/(A_{pi} + A_{Fi})$, where A_{Fi} is the surface of fractures for the ith fragment and A_{Pi} is the original area of the ith fragment at the pore interface.

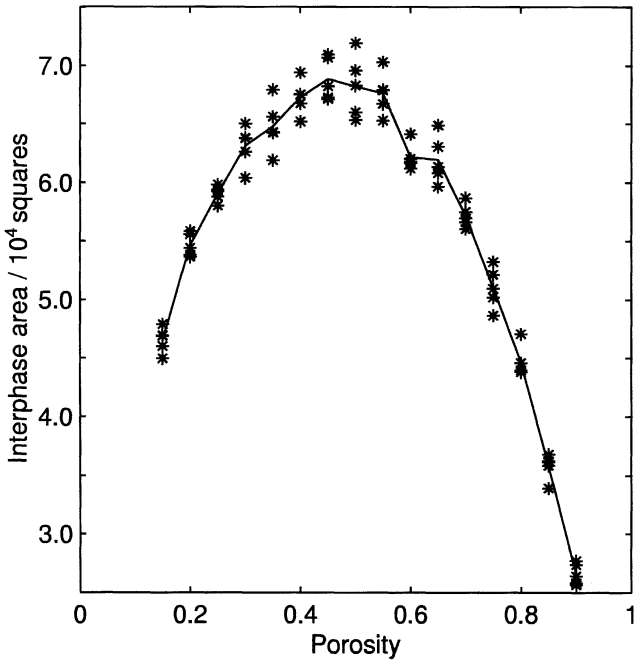

Figure 7. Dependence of the interphase area, that is, the total surface area of the solid phase, on the porosity of the catalyst sample (before its fragmentation).

The porous structure was reconstructed five times for each value of porosity.

The cross-section area of the solid-phase perpendicular to the skeleton edge is calculated along all skeleton branches of the solid phase. The solid phase is then disconnected at the points corresponding to the absolute minima of that cross-section area for every skeleton edge (Liang et al., 2000a). The illustration of this method is shown in Figure 3.

Results of catalyst fragmentation

Several samples of porous media have been reconstructed to test and compare our fragmentation algorithms. The overview of results is shown in Table 2. Since it is difficult to visualize the fragmentation of the cube composed of $64 \times 64 \times 64$ voxels (samples A and D), the slices of this cube with the dimension $64 \times 64 \times 8$ were also processed for illustration. The skeleton of the solid phase obtained by the conditional thinning algorithm, fractures predicted by the skeleton disconnection, and by the Delaunay tessellation algorithm with the "Manhattan" or "Chessboard" metrics are presented for two selected samples in Figures 4 and 5. Several characteristic distributions of fragments are shown in Figure 6.

The results of Delaunay triangulation with "Chessboard" metrics appear to be close to typical fracture images. The same fragmentation method with the "Manhattan" metrics provides a large number of very small fragments. Let us recall that the number of fragments depends on the number of local maxima in the function $T(\boldsymbol{x})$ specifying the distance of the solid element from the nearest pore. The algorithm based on the skeleton disconnection is limited by the strict requirement of planar fractures. Therefore, the fragmentation for this algorithm looks quite artificial, especially for samples with a low porosity.

A number of porous samples with the same correlation function, but with a varying porosity, has been reconstructed and analyzed by our algorithms. The size of all these samples was $64 \times 64 \times 64$. The interphase area, that is, the surface of pores depends on porosity, as can be seen from Figure 7. This area is assumed to be covered by the catalytically active sites, while the area of newly formed fractures is catalytically inactive. The dependence of the interphase area on the porosity has a maximum at the porosity of 0.5 for the reconstructed porous media.

The dependence of the newly formed fractures on the porosity obtained for every fragmentation algorithm is shown in Figure 8. The used algorithms provide significantly different predictions at low porosities, while the results for porosities larger than 0.5 are similar. A qualitatively different output of the skeleton disconnection is observed for small porosities and the area vs. porosity dependence of this algorithm has a maximum. The total area of fractures predicted by tessellation with "Chessboard" and "Manhattan" metrics decreases along the porosity axis.

The dependence of the number of fragments on the porosity is shown on Figure 9, and this dependence has a flat maximum. High variance of the results obtained for several reconstructed porous media can be observed, especially in the case of skeleton disconnection. The possibility of a reduction of this variance by increasing the dimension of reconstructed samples is going to be the subject of simulations on larger parallel computers.

The average activity of fragment surfaces is displayed in Figure 10. Here, the activity of a fragment is defined as the

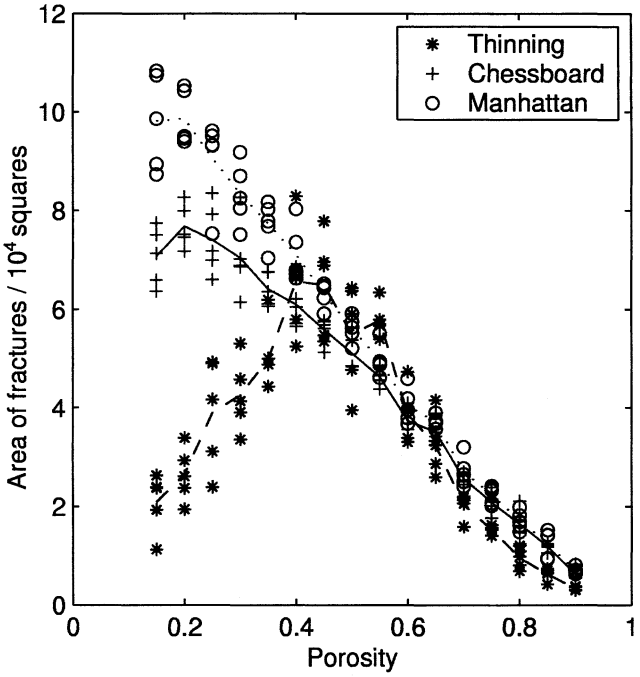

Figure 8. Dependence of the area of fractures formed by the fragmentation on the porosity of the catalyst sample for the three considered algorithms, where "Thinning" is the skeletonization-based method, and "Chessboard" and "Manhattan" are Delaunay tessellations with respective metrics.

The porous structure was reconstructed five times for each value of porosity.

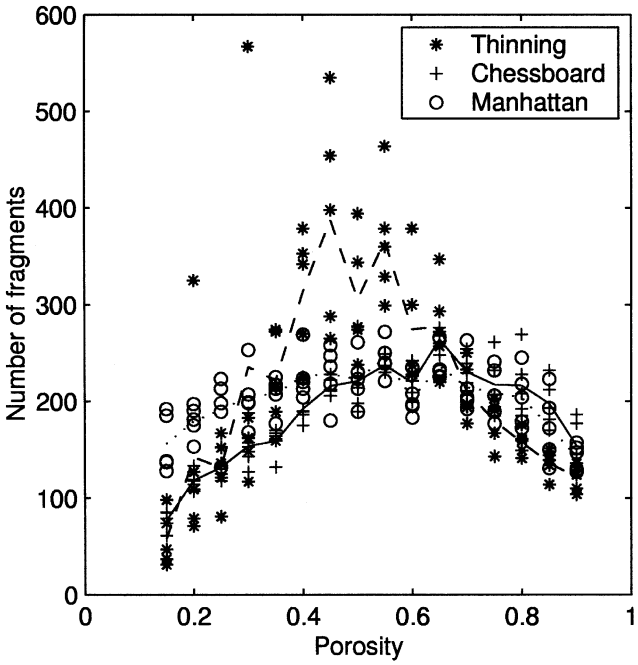

Figure 9. Dependence of the number of fragments on the porosity of the catalyst sample for the three considered algorithms, where "Thinning" is the skeletonization-based method, and "Chessboard" and "Manhattan" are Delaunay tessellations with respective metrics.

The porous structure was reconstructed five times for each value of porosity.

ratio $A_P/(A_P + A_F)$, where A_P is the area of the solid–pore interface before the fragmentation started (that is, the area potentially covered by active catalyst species) and A_F is the area of the newly formed fractures. We can again observe a qualitative difference among the results of skeletonization algorithm and predictions by the other two algorithms for porosities lower than 0.3, but satisfactory agreement for higher values of porosity. As the porosities of catalyst carriers are usually large, we can conclude that the agreement among the predictions is satisfactory for practical values of porosities.

Our calculations show that the dependence of surface area accessible to active catalyst sites A_P on porosity ϵ has a maximum for porosity around $\epsilon = 0.5$. The large porosity generally allows for an easier fragmentation and faster transport through the porous structure, but the "active" surface area A_P is small. On the other hand, the catalyst support with a small porosity is more difficult to fragment since the newly formed surface of fractures A_F is large. However, experimental data indicate that the mean pore diameter and other characteristics of porous catalyst carriers are also important for catalyst performance (Furtek, 1987).

Conclusions and Prospects

This work illustrated the usefulness of pore space reconstruction as a mean of relating effective transport properties of porous catalyst and polymer particles to the geometry and topology of the pore phase obtained from microscopy images. Effective transport properties are calculated with no tunable parameters and effective mechanical properties could be also calculated (Adler and Thovert, 1998). However, predictions of transport properties could be somewhat inaccurate because of the inability of simple reconstruction methods to accurately reflect the contributions of pores smaller than the considered spatial resolution of the system. The problem of porous materials with broad pore-size distributions is addressed, for example, by Mourzenko et al. (2001).

The output of the fragmentation analysis are the positions of the fragments in the space and the size, area, and activity of each fragment. These results can be used as input parameters to the next stage of particle morphology modeling. One catalyst fragment forms the core of the so-called micrograin in the multigrain concept, where the catalyst fragment is surrounded by the layer of the produced polymer. The growth of micrograins and mutual viscoelastic interactions between the micrograins have to be simulated in order to describe the evolution of particle morphology, and the effective transport properties in the polymer particle could be calculated simultaneously (Grof et al., 2001). The problem of particle morphogenesis was also studied by the effective-scale model employing the buildup and relaxation of elastic tensions inside growing particles (Kittilsen et al., 2001).

The porous structure of the catalyst/polymer particles in the early stage of its growth could be alternatively represented by the agglomerate of spherical microelements of two

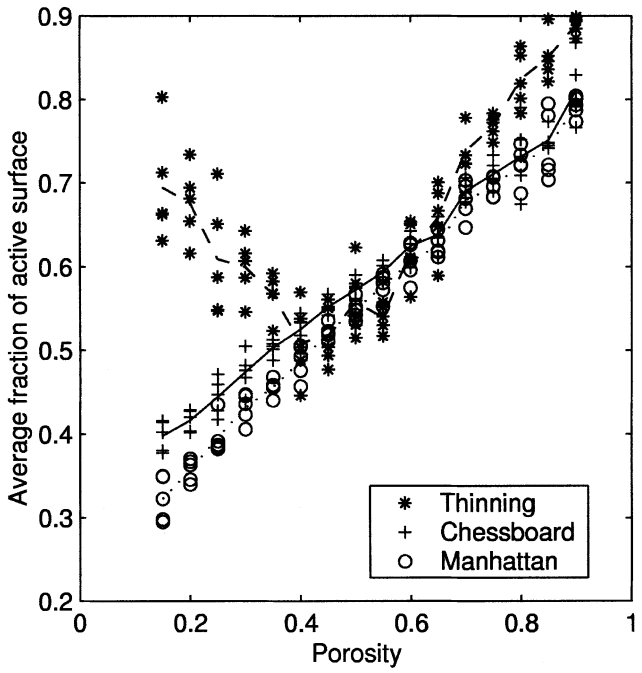

Figure 10. Dependence of the average fraction of fragment surfaces covered by the catalyst on the porosity of the catalyst sample for the three considered algorithms, where "Thinning" is the skeletonization-based method, and "Chessboard" and "Manhattan" are Delaunay tessellations with respective metrics.

The porous structure was reconstructed five times for each value of porosity.

types representing the catalyst and polymer phases. Microelements considered are subjected to elastic and viscoelastic interactions. A mathematical model based on such a representation also takes into account the time scale of the fragmentation and the magnitude of stresses causing the fracturing of catalyst support.

It is questionable whether the observations made in carefully controlled experiments performed under mild conditions of slow polymerization are applicable to typical process conditions in industrial reactors. The modeling could thus become a powerful tool suitable for analysis of fragmentation processes at faster polymerization rates.

Scarce experimental data are available on the distribution of active catalyst sites (or potential sites as their precursors) in porous carriers. Strong experimental input required for our modeling studies could benefit from controlled experiments, such as from the specifically designed distribution of active catalyst on the silica substrate (Goretzki et al., 1999; Thüne et al., 1997). Polymerization of olefins on zeolite supports, such as ZSM-5 or MCM-41, with a well-defined pore structure and a narrow pore-size distribution, could also bring significant progress to the understanding of catalyst fragmentation (Vayá et al., 2001).

Acknowledgments

Financial support from the Czech Grant Agency (projects GA ČR 104/02/0339 and 104/02/0325), from the French-Czech Barrande project No. 2000-008-3 and from the ESF project "Reactor" is gratefully acknowledged. Z. Grof would like to acknowledge the support of the European Commission (Grant number HPRI-CT-1999-00026, TRACS Programme at EPCC). Special thanks for stimulating discussions belong to František Štěpánek.

Literature Cited

Adler, P. M., *Porous Media: Geometry and Transports*, Butterworth/Heineman, Stoneham, MA (1992).

Adler, P. M., and J. F. Thovert, "Real Porous Media: Local Geometry and Macroscopic Properties," *Appl. Mech. Rev.*, **51**, 537 (1998).

Arns, C. H., M. A. Knackstedt, W. V. Pinczewski, and K. R. Mecke, "Euler-Poincaré Characteristics of Classes of Disordered Media," *Phys. Rev. E*, **63**, 031112 (2001).

Bekri, S., K. Xu, F. Yousefian, P. M. Adler, J. F. Thovert, J. Muller, K. Iden, A. Psyllos, A. K. Stubos, and M. A. Ioannidis, "Pore Geometry and Transport Properties in North Sea Chalk, *J. of Pet. Sci. and Eng.*, **25**, 107 (2000).

Biswal, B., C. Manwart, R. Hilfer, S. Bakke, and P. E. Oren, "Quantitative Analysis of Experimental and Synthetic Microstructures for Sedimentary Rock," *Physica A*, **273**, 462 (1999).

Bonini, F., V. Fraaije, and G. Fink, "Propylene Polymerization through Supported Metallocene/MAO Catalysts: Kinetic Analysis and Modelling," *J. Poly. Sci.: Part A: Poly. Chem.*, **33**, 2393 (1995).

Conner, W. C., S. W. Webb. P. Spanne, and K. W. Jones, "Use of X-ray Microscopy and Synchrotron Microtomography to Characterize Polyethylene Polymerization Particles," *Macromolecules*, **23**, 4742 (1990).

Debling, J. A., and W. H. Ray, "Heat and Mass Transfer Effects in Multistage Polymerization Processes: Impact Polypropylene," *Ind. Eng. Chem. Res.*, **34**, 3466 (1995).

Debling, J. A., and W. H. Ray, "Morphological Development of Impact Polypropylene Produced in Gas Phase with a $TiCl_4/MgCl_2$ Catalyst," *J. Appl. Poly. Sci.*, **81**, 3085 (2001).

dos Santos, J. H. Z., H. T. Ban, T. Teranishi, T. Uozumi, T. Sano, K. Soga, "Indenyl-Silica Xerogels: New Materials for Supporting Metallocene Catalysts," *Appl. Catalysis A: General*, **220**, 287 (2001).

Estenoz, D. A., and M. G. Chiovetta, "A Structural Model for the Catalytic Polymerization of Ethylene Using the Chromium Catalysts: I. Description and Solution," *Poly. Eng. Sci.*, **36**, 2208 (1996).

Estenoz, D. A., and M. G. Chiovetta, "Olefin Polymerization Using Supported Metallocene Catalysts: Process Representation Scheme and Mathematical Model," *J. Appl. Poly. Sci.*, **81**, 285 (2001).

Ferrero, M. A., and M. G. Chiovetta, "Catalyst Fragmentation During Propylene Polymerization: I. The Effects of Grain Size and Structure," *Poly. Eng. Sci.*, **27**, 1436 (1987).

Ferrero, M. A., E. Koffi, R. Sommer, and W. C. Conner, "Characterization of the Changes in the Initial Morphology for $MgCl_2$-Supported Ziegler-Natta Polymerization Catalysts," *J. Poly. Sci.: Part A: Poly. Chem.*, **30**, 2131 (1992).

Ferrero, M. A., R. Sommer, P. Spanne, K. W. Jones, and W. C. Conner, "X-Ray Microtomography Studies of Nascent Polyolefin Particles Polymerized over Magnesium Chloride-Supported Catalysts," *J. Poly. Sci.: Part A: Poly. Chem.*, **31**, 2507 (1993).

Fink, G., B. Tesche, F. Korber, and S. Knoke, "The Particle-Forming Process of SiO_2-Supported Metallocene Catalysts," *Macromol. Symp.*, **137**, 77 (2001).

Floyd, S., K. Y. Choi, T. W. Taylor, and W. H. Ray, "Polymerization of Olefins through Heterogeneous Catalysis: III. Polymer Particle Modeling with an Analysis of Intraparticle Heat and Mass Transfer Effects," *J. Appl. Poly. Sci.*, **32**, 2935 (1986).

Furtek, A. B., "Catalyst Composition for Polymerizing Alpha-Olefins," U.S. Patent No. 4,670,413 (1987).

Galli, P., and J. C. Haylock, "Advances in Ziegler-Natta Polymerization—Unique Polyolefin Copolymers, Alloys and Blends made Directly in the Reactor," *Makromol. Chem., Macromol. Symp.*, **63**, 19 (1992).

Galli, P., "The Breakthrough in Catalysis and Processes for Olefin Polymerization: Innovative Structures and a Strategy in the Materials Area for the Twenty-First Century," *Prog. Poly. Sci.*, **19**, 959 (1994).

Galvan, R., and M. Tirrell, "Orthogonal Collacation Applied to

Analysis of Heterogeneous Ziegler-Natta Polymerization," *Comput. Chem. Eng.*, **10**, 77 (1986).
Goretzki, R., G. Fink, B. Tesche, B. Steinmetz, R. Rieger, and W. Uzick, "Unusual Ethylene Polymerization Results with Metallocene Catalysts Supported on Silica," *J. Poly. Sci.: Part A: Poly. Chem.*, **37**, 677 (1999).
Grof, Z., J. Kosek, A. Novák, and M. Marek, "Meso-scopic Modeling of Morphogenesis of Polyolefin Particles in Heterogenous Catalytic Reactors," *Int. Workshop on Poly. React. Eng.*, Hamburg, Germany, H.-U. Moritz, and K.-H. Reichert, eds., Wiley VCH, Weinheim, 61 (2001).
Hazlett, R. D., "Statistical Characterization and Stochastic Modeling of Pore Networks in Relation to Fluid Flow," *Mathematical Geology*, **29**, 801 (1997).
Hoel, E. L., C. Cozewith, and G. D. Byrne, "Effect of Diffusion on Heterogeneous Ethylene Propylene Copolymerization," *AIChE J.*, **40**, 1669 (1994).
Hutchison, R. A., and W. H. Ray, "Polymerization of Olefins through Heterogeneous Catalysis: VII. Particle Ignition and Extinction Phenomena," *J. Appl. Poly. Sci.*, **34**, 657 (1987).
Kakugo, M., H. Sadatoshi, J. Sakai, and M. Yokoyama, "Growth of Polypropylene Particles in Heterogeneous Ziegler-Natta Polymerization," *Macromolecules*, **22**, 3172 (1989).
Kittilsen, P., T. F. McKenna, H. Svendsen, H. A. Jakobsen, and S. B. Fredriksen, "The Interaction between Mass Transfer Effects and Morphology in Heterogeneous Olefin Polymerization," *Chem. Eng. Sci.*, **56**, 4015 (2001).
Kosek, J., Z. Grof, A. Novák, F. Štěpánek, and M. Marek, "Dynamics of Particle Growth and Overheating in Gas-Phase Polymerization Reactors," *Chem. Eng. Sci.*, **56**, 3951 (2001a).
Kosek, J., F. Štěpánek, A. Novák, Z. Grof, and M. Marek, "Multi-Scale Modelling of Growing Polymer Particles in Heterogeneous Holding Catalytic Reactors," *Euro. Symp. on Comput. Aided Process Eng.*, **11**, R. Gani, and S. B. Jørgensen, eds., Elsevier, Amsterdam, 177 (2001b).
Krishna, R., and J. A. Wesseling, "The Maxwell-Stefan Approach to Mass Transfer," *Chem. Eng. Sci.*, **52**, 861 (1997).
Kurumada, K., H. Nakabayashi, T. Murataki, and M. Tanigaki, "Structure and Formation Process of Silica Microparticles and Monolithic Gels Prepared by the Sol-Gel Method," *Colloid and Surfaces A: Physicochemical and Engineering Aspects*, **139**, 163 (1998).
Liang, Z., M. A. Ioannidis, and I. Chatzis, "Geometric and Topological Analysis of Three-Dimensional Porous Media: Pore Space Partitioning Based on Morphological Skeletonization," *J. Colloid Interface Sci.*, **221**, 13 (2000a).
Liang, Z., M. A. Ioannidis, and I. Chatzis, "Permeability and Electrical Conductivity of Porous Media from 3D Stochastic Replicas of the Microstructure," *Chem. Eng. Sci.*, **55**, 5247 (2000b).
Ma, M. C., and M. Sonka, "A Fully Parallel 3D Thinning Algorithm and its Applications," *Computer Vision and Image Understanding*, **64**(3), 420 (1996).
McDaniel, M. P., "Fracturing Silica-Based Catalysts During Ethylene Polymerization," *J. Poly. Sci., Poly. Chem. Ed.*, **19**, 1967 (1981).
McDaniel, M. P., "Supported Chromium Catalysts for Ethylene Polymerization," *Advan. in Catal.*, **33**, 47 (1985).
McDaniel, M. P., D. R. Witt, and E. A. Benham, "The Effect of Alkali Metal Doping on the Performance of Cr/Silica Catalysts in Ethylene Polymerization," *J. Catal.*, **176**, 344 (1998).
McKenna, T. F., J. Dupuy, and R. Spitz, "Modeling of Transfer Phenomena on Heterogeneous Ziegler Catalysts: III. Modeling of Intraparticle Mass Transfer Resistance," *J. Appl. Poly. Sci.*, **63**, 315 (1997).
McKenna, T. F., D. Cokljat, R. Spitz, and D. Schweich, "Modelling of Heat and Mass Transfer during the Polymerisation of Olefins on Heterogeneous Ziegler Catalysts," *Catal. Today*, **48**, 101 (1999).
Mourzenko, V. V., J. F. Thovert, and P. M. Adler, "Percolation in Two-Scale Porous Media," *Eur. Phys. J. B*, **19**, 75 (2001).
Muñoz-Escalona, A., J. G. Hernandez, and J. A. Gallardo, "Catalytic Activity and Control of the Nascent Morphology and Polyethylenes Obtained with First and Second Generation of Ziegler-Natta Catalysts," *J. Appl. Poly. Sci.*, **29**, 1187 (1984).
Niegisch, W. D., S. T. Crisafulli, T. S. Nagel, and B. E. Wagner, "Characterization Techniques for the Study of Silica Fragmentation in the Early Stages of Ethylene Polymerization," *Macromolecules*, **25**, 3910 (1992).
Noristi, L., E. Marchetti, G. Baruzzi, and P. Sgarzi, "Investigation on the Particle Growth Mechanism in Propylene Polymerization with $MgCl_2$-Supported Ziegler-Natta Catalysts," *J. Poly. Sci.: Part A: Poly. Chem.*, **32**, 3047 (1994).
Pater, J. T. M., G. Weickert, J. Loos, and W. P. M. van Swaaij, "High Precision Prepolymerization of Propylene at Extremely Low Reaction Rates—Kinetics and Morphology," *Chem. Eng. Sci.*, **56**, 4107 (2001).
Ruddick, V. J., and J. P. S. Badyal, "AFM Study of the Breakup of Catalyst Particles during Ethylene Polymerization," *J. Phys. Chem. B.*, **101**, 1791 (1997).
Sliepcevich, A., G. Storti, and M. Morbidelli, "Measurement of Diffusivity and Solubility of Olefins in Polypropylene by Gas Chromatography," *J. Appl. Poly. Sci.*, **78**, 464 (2000).
Steinmetz, B., B. Tesche, C. Przybyla, J. Zechlin, and G. Fink, "Polypropylene Growth on Silica-Supported Metallocene Catalysts: A Microscopic Study to Explain Kinetic Behavior Especially in Early Polymerization Stages," *Acta Polym.*, **48**, 392 (1997).
Štěpánek, F., M. Kubíček, M. Marek, and P. M. Adler, "Computer-Aided Screening of Adsorbents and Porous Catalyst Carriers," *European Symp. on Comput. Aided Process Eng. 10*, Florence, Italy, S. Pierucci, ed., Elsevier Science, Amsterdam, 667 (2000).
Thornton, C., M. T. Ciomocos, and M. J. Adams, "Numerical Simulations of Agglomerate Impact Breakage," *Powder Technol.*, **105**, 74 (1999).
Thovert, J. F., J. Salles, and P. M. Adler, "Computerized Characterization of the Geometry of Real Porous Media: Their Discretization, Analysis and Interpretation," *J. Microsc.*, **170**, 65 (1993).
Thovert, J. F., F. Yousefian, P. Spanne, C. G. Jacquin, and P. M. Adler, "Grain Reconstruction of Porous Media: Application to a Low-Porosity Fontainebleau Sandstone," *Phys. Rev. E*, **63**, 061307 (2001).
Thüne, P. C., C. P. J. Verhagen, M. J. G. van den Boer, and J. W. Neimantsverdriet, "Working Surface Science Model for the Phillips Ethylene Polymerization Catalyst: Preparation and Testing," *J. Phys. Chem. B*, **101**, 8559 (1997).
Vayá, V. I. C., P. G. Belelli, J. H. Z. dos Santos, M. L. Ferreira, and D. E. Damiani, "Influence of Acidic Support in Metallocene Catalysts for Ethylene Polymerization," *J. Catal.*, **204**, 1 (2001).
Weckhuysen, B. M., and R. A. Schoonheydt, "Olefin Polymerization over Supported Chromium Oxide Catalysts," *Catalysis Today*, **51**, 215 (1999).
Weist, E. L., A. H. Ali, B. G. Naik, and W. C. Conner, "Morphological Study of Supported Chromium Polymerization Catalysts. 2. Initial Stages of Polymerization," *Macromolecules*, **22**, 3244 (1989).
Yeong, C. L. Y., and S. Torquato, "Reconstructing Random Media," *Phys. Rev. E*, **57**, 495 (1998).
Zechlin, J., B. Steinmetz, B. Tesche, and G. Fink, "Development of a Refined Poly(propylene) Growth Model for Silica Supported Metallocene Catalyst Systems," *Macromol. Chem. Phys.*, **201**, 515 (2000).

Manuscript received Apr. 16, 2002, and revision received Sept. 24, 2002.